On inherent spatio-spectral image distortion in AOTF-based imagers

Martynov, Grigoriy, Gorevoy, Alexey, Machikhin, Alexander, Pozhar, Vitold

Grigoriy N. Martynov, Alexey V. Gorevoy, Alexander S. Machikhin, Vitold E. Pozhar, "On inherent spatio-spectral image distortion in AOTF-based imagers," Proc. SPIE 11782, Optical Measurement Systems for Industrial Inspection XII, 1178219 (20 June 2021); doi: 10.1117/12.2592557

SPIE.

Event: SPIE Optical Metrology, 2021, Online Only

On inherent spatio-spectral image distortion in AOTF-based imagers

Grigoriy N. Martynov, Alexey V. Gorevoy, Alexander S. Machikhin, and Vitold E. Pozhar

Laboratory of Acousto-optic Spectroscopy, Scientific and Technological Center of Unique Instrumentation, Russian Academy of Sciences, 15 Butlerova str., Moscow 117342, Russia

ABSTRACT

Acousto-optical tunable filters (AOTFs) based on interaction of light and ultrasound in uniaxial birefringent crystals are widely used in imaging spectroscopy applications due to random spectral access, narrow controllable bandwidth, compactness, overal ease-of-use and image trasmittance capability. The spectral transmission of AOTF-based spectral imagers is usually characterized for paraxial light beam, but AOTFs inherently have non-uniform spatio-spectral transmission, so the central wavelength of the transmission window varies with the angle of incident light. We demonstrate that the spatio-spectral characteristics of acousto-optic (AO) interaction may be described either by the dependency of ultrasound frequency on the incident light angle for a given wavelength or by the dependency of wavelength on the incident angle for a given sound frequency. These dependencies are derived from the phase matching condition and are determined by the refractive indices, sound phase velocities and the AO diffraction geometry. We experimentally estimate the appearance of this specific spatio-spectral structure on the images acquired by AOTF-based imagers based on both collimating and confocal (telecentric) schemes and show that the variations of central wavelength and spectral bandwidth are noticeable for collimating setup even in the commonly used small field of view. The results of the study may be applied in design of AOTF-based spectral imagers and image processing algorithms.

Keywords: acoutso-optics, acousto-optical tunable filters, hyperspectral imaging, digital image processing

1. INTRODUCTION

Acousto-optical tunable filters (AOTFs) are optical filters based on interaction of light and ultrasound in crystalline media that provides spectrally selective Bragg diffraction. Their remarkable properties, such as random access spectral tunability by applied driving signal, narrow and controllable bandwidth, compactness, capability to filter image-carrying beams and overall ease-of-use made them a very important spectroscopic tool and one of the major hyperspectral imaging (HSI) technologies. AOTF-based imagers have found their use in various devices and laboratory setups used for bioimaging, agricultural and enviromental monitoring, thermometry, food quality control, astronomy, space studies and other fields of research.[1–13]

Despite AOTFs are widespread element of spectral imaging devices, their features and characteristics, which can affect quality of filtered image, are not fully taken into consideration. AOTFs utilize the three-wave interaction of incident and diffracted light coupled by ultrasound and their operation is described by the Bragg diffraction phase-matching condition derived from the momentum conservation law.[14] Therefore, the transmission of any AOTF depends on the wavelength λ of incident light, ultrasound frequency f and the incident angle of light, so the transmission function exhibits a pronounced spatio-spectral character. Such a behaviour has led to many interesting applications like spatial filtering of images,[15,16] laser beam shaping[17] and AOTF-masked phase microscopy,[9] which utilize the change in angular transmission function of light from monochromatic light source with the change in ultrasound frequency. The other side of this effect is the variation of the central wavelength of the spectral transmission window with the angle of incident light. Sadly, the majority of prior studies and designs of AOTF-based imagers ignored this effect and relied on the AOTF tuning relationship $\lambda(f)$ traditionally obtained for the paraxial rays as the standard characterization methods prescribe.[18] In fact, such an

Further author information: (Send correspondence to A.S.M.)
A.S.M.: E-mail: machikhin@ntcup.ru

Optical Measurement Systems for Industrial Inspection XII, edited by Peter Lehmann, Wolfgang Osten, Armando Albertazzi Gonçalves, Proc. of SPIE Vol. 11782, 1178219
 · doi: 10.1117/12.2592557

approach may lead to inaccurate results and the emergence of recent works[12,19,20] addressing this issue indicates a growing interest in it.

The spatio-spectral transmission function of AOTF follows from the phase matching condition and is determined by the refractive indices, sound phase velocities and the acousto-optic (AO) diffraction geometry, so we can predict, model and correct all the unwanted effects or at least be aware of them. In this work, we analyze the spatio-spectral characteristics for wide-aperture non-collinear AO interaction in paratellurite (TeO_2) crystal using computer modeling, experimentally evaluate spatio-spectral inhomogeneities for the most popular collimating and confocal telecentric schemes of AOTF-based spectral imager and finally perform a monochromatization of spectrally non-uniform images obtained with a collimating setup.

2. SPATIO-SPECTRAL CHARACTERISTICS OF ACOUSTO-OPTIC INTERACTION

The basic laws that govern the AO interaction are phase-matching conditions originating from the laws of energy and momentum conservation. In practice, frequency shifts introduced by ultrasound are small compared to optical frequencies, so the wavelengths of incident λ_{i0} and diffracted λ_{d0} light in vacuum are usually considered equal $\lambda_{i0} \approx \lambda_{d0} = \lambda_0$ and the analysis of AO diffraction geometry may be conducted using the equation for wavevectors $\mathbf{k}_d = \mathbf{k}_i \pm \mathbf{q}$. This equation may be presented in the expanded form:

$$[n_d(\lambda_{d0}, \mathbf{e}_{kd})/\lambda_{d0}]\,\mathbf{e}_{kd} = [n_i(\lambda_{i0}, \mathbf{e}_{ki})/\lambda_{i0}]\,\mathbf{e}_{ki} \pm [f/V(\mathbf{e}_q)]\,\mathbf{e}_q, \quad (1)$$

where $\mathbf{e}_q$, $\mathbf{e}_{ki}$ and $\mathbf{e}_{kd}$ are the unit vectors indicating directions of wavevectors $\mathbf{q}, \mathbf{k}_i$ and $\mathbf{k}_d$ for sound, incident and diffracted light; V is the sound velocity; n_i and n_d are the refractive indices of the medium before and after the diffraction. We consider non-collinear anisotropic (e→o) AO interaction in tetragonal uniaxial crystal where $n_i = n_e$, $n_d = n_o$ and $\mathbf{e}_q$ is defined by the cut angle γ (see Fig. 1a). The length of vectors $\mathbf{k}_i$ and $\mathbf{k}_d$ depends on the refractive indices $n_o(\lambda_0)$ and $n_e(\lambda_0)$; the wavenumber k_0 corresponds to light wavelength in vacuum: $k_0 = 2\pi/\lambda_0$.

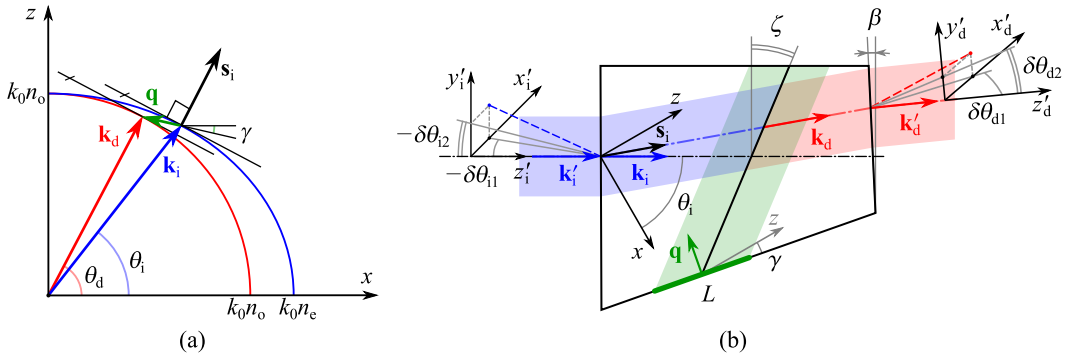

Figure 1. Wavevector diagram (a) and AO cell configuration (b) for non-collinear anisotropic (e → o) AO interaction in a uniaxial crystal.

Widely-used approach to the design of AOTF for spectral imaging applications relies on the wide-aperture configuration of AO interaction,[1] where the phase matching condition is approximately satisfied over a wide range of incident light angles θ. It is achievable when the tangents to the wave surfaces for incident and diffracted light are parallel, or, equivalently, the directions of light propagation $\mathbf{s}_i$ and $\mathbf{s}_d$ (group velocities) are parallel. This condition for anisotropic (e→o) AO diffraction may be written as the relations between the incident angles of light θ_i, θ_d and the sound angle γ in the polar plane xz.[21,22] In this work, we choose the light and sound angles accordingly. The following analysis is performed for TeO_2 crystal (the most widely used uniaxial birefringent crystal for AOTF), but the most results are applicable to other tetragonal uniaxial crystals. For TeO_2 x and z axes correspond to [110] and [001] axes.

In order to describe the transformation of the light beam on its way through the AO cell, we introduce the mathematical model of AO cell including three surfaces: input facet, intermediate diffraction plane and output facet[12,19,23,24] as shown in Fig. 1b. The input coordinate system $x'_i y'_i z'_i$ is defined so that z'_i-axis is parallel to the wavevector $\mathbf{k}_i$, which exactly satisfies the phase matching condition for a given wavelength λ_s. We assume that the input facet of the AO cell is perpendicular to z'_i-axis, so the wavevectors $\mathbf{k'}_i$ and $\mathbf{k}_i$ are collinear. The angles $\delta\theta_{i1}$ and $\delta\theta_{i2}$ define the directions of other rays inside the incident light beam and their wavevectors. In order to simplify the description in this paper, we assume that the plane $y'_i z'_i$ and the polar plane xz coincide and that all three surfaces are parallel to x'_i-axis.

The wavevector $\mathbf{k}_i$ and the light propagation vector $\mathbf{s}_i$ after the refraction of the extraordinary wave on the input facet are calculated for given vector $\mathbf{k}'_i$ using the equations provided in Ref. 25. The ray is propagated along $\mathbf{s}_i$ in the crystal to the intermediate diffraction plane, which is assumed to be approximately at the center of piezotransducer. Its tilt angle ζ depends on cut angle γ and acoustic walk-off angle in TeO_2 as[26]

$$\zeta = \arctan\left(\left(V_{001}/V_{110}\right)^2 \tan\gamma\right) + \theta_i - \pi/2, \tag{2}$$

where V_{001} and V_{110} are the sound phase velocities along the corresponding axes. The acoustic frequency f satisfying Eq. (1) for a wavelength λ may be calculated as follows:[19,27]

$$f = V(\mathbf{e}_q) n_o(\lambda) \left[\xi A - \sqrt{\xi^2 (A^2 - 1) + 1}\right] / \lambda, \tag{3}$$

$$\xi = n_e(\lambda) / \sqrt{n_o^2(\lambda)\cos^2\theta_i + n_e^2(\lambda_0)\sin^2\theta_i}, \tag{4}$$

where ξ is a birefringence parameter and A is a geometrical parameter, $A = -\mathbf{e}_{ki} \cdot \mathbf{e}_q$. Thus, we can calculate the ultrasound frequency f_s required to satisfy the phase matching condition for the axial ray $\mathbf{k}_i$ at a given wavelength λ_s. The equation for the sound phase velocity $V(\gamma)$ may be found in Ref. 26. Next, we find the corresponding sound wavevector $\mathbf{q}$ as $\mathbf{q} = [f_s/V(\mathbf{e}_q)]\,\mathbf{e}_q$ and the wavevector for diffracted light as $\mathbf{k}_d = \mathbf{k}_i + \mathbf{q}$. We should not that the direction of light propagation for the wide-aperture geometry does not change after the AO diffraction, so $\mathbf{k}_d$, $\mathbf{s}_d$ and $\mathbf{s}_i$ are collinear. Finally, the ray is traced to the output facet and the wavevector $\mathbf{k}'_d$ in the air is calculated using the basic refraction law for the ordinary wave. The tilt angle of the output facet β may be chosen to provide normal incidence of the axial beam or to minimize chromatic aberrations.[23] The output coordinate system $x'_d y'_d z'_d$ is defined as the input system $x'_i y'_i z'_i$ rotated about x'_i-axis so the output wavevector $\mathbf{k}'_d$ is parallel to z'_d-axis (Fig. 1b). As well as before, we introduce angles $\delta\theta_{d1}$ and $\delta\theta_{d2}$, which characterize other rays inside the output diffracted light beam and are measured from the axial ray.

If we consider some direction of incident ray defined by angles $(\delta\theta_{i1}, \delta\theta_{i2})$, we can similarly find the ultrasound frequency f required to satisfy the phase matching condition for this ray at the same wavelength λ_s using Eq. (3). In TeO_2 these frequencies f are higher than the frequency f_s for the axial ray. This may be illustrated by the wavevector diagram shown in Fig. 2a. The same frequency f also complete the phase matching for other wavevector directions, which form a ring-like curve on the wavevector surfaces. We can calculate the distribution $f(\delta\theta_{i1}, \delta\theta_{i2})$ (see Fig. 2b), which represents the phase-matching locus in the input angular coordinates for a given wavelength λ_s. The calculation were made for TeO_2 crystal with cut angle $\gamma = 7°$ and wide-aperture geometry with $\theta_i = 73.85°$ at $\lambda_s = 650$ nm. The locus has the shape similar to a paraboloid, but it is asymmetric about the vertical axis in the plane $\delta\theta_{i1} = 0$. Horizontal sections of this surface define the incident light directions with maximum transmission for each f. This dependency is actively used for applications with monochromatic light sources like spatial filtering of images or laser beam shaping,[15,28] but it also appears in spectral imaging application as a variation of spectral transmission function with pixel coordinates (u, v) of image $I(u, v, f)$.

Alternatively, we can solve Eq. (3) for any input direction $(\delta\theta_{i1}, \delta\theta_{i2})$ and a given frequency f_s and find the wavelength λ, which exactly satisfies the phase matching condition. As shown in Fig. 2d, the solution can be found for lower values of refraction indices and, consequently, longer wavelengths λ than λ_s. The distribution $\lambda(\delta\theta_{i1}, \delta\theta_{i2})$ (see Fig. 2e) represents the phase-matching locus for a given acoustic frequency f_s and has the shape similar to $f(\delta\theta_{i1}, \delta\theta_{i2})$. As a result, the spatio-spectral inhomogeneity of AOTF may be described either by the dependency $f(\delta\theta_{i1}, \delta\theta_{i2})$ at a given wavelength λ_s or by the dependency $\lambda(\delta\theta_{i1}, \delta\theta_{i2})$ at a given frequency f_s. Using the ray tracing model described above, these dependencies may be presented in the output

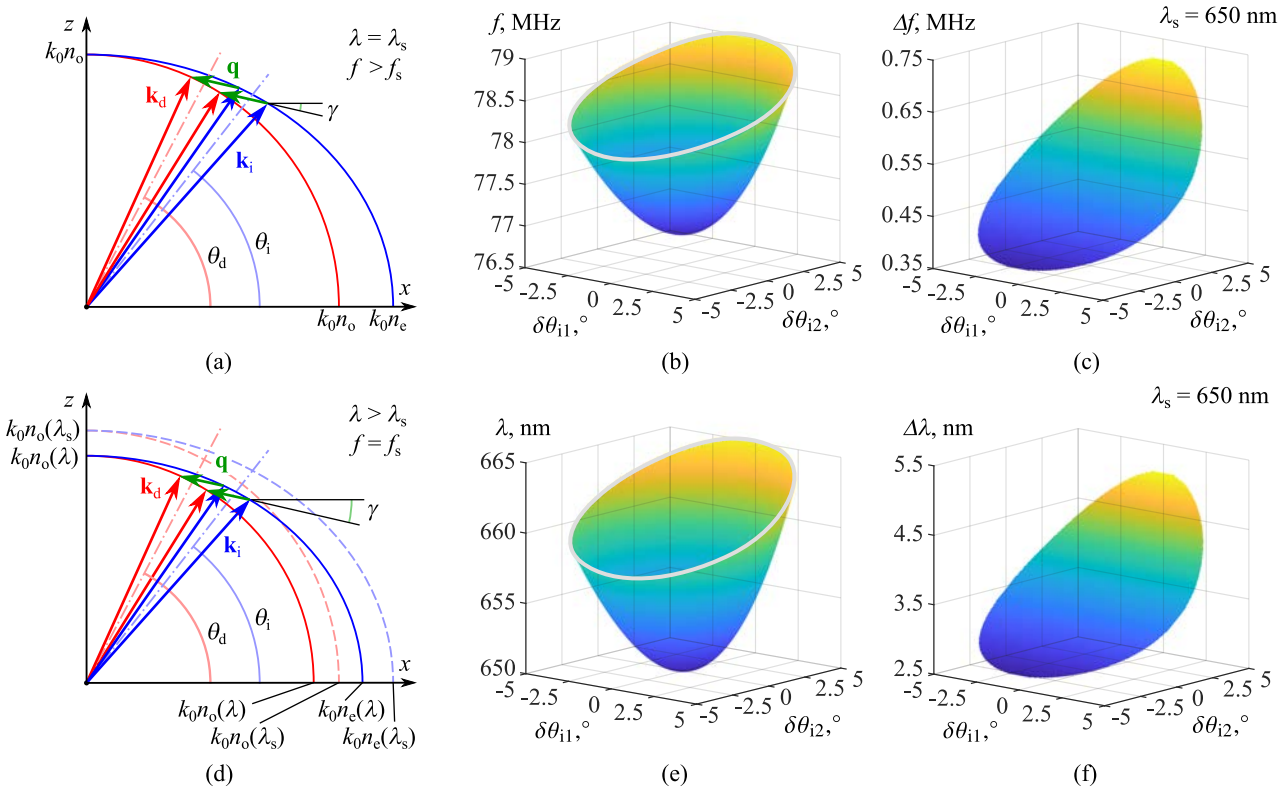

Figure 2. Spatio-spectral characteristics of AO interaction. Wavevector diagram (a) illustrating phase matching condition for different ultrasound frequencies $f > f_s$ at given wavelength $\lambda_s = 650$ nm, distributions of frequency f corresponding to exact synchronism (b) and frequency bandwidth Δf (FWHM) (c) across the circular FOV $\pm 5°$ in TeO_2 crystal with $\gamma = 7°$. Wavevector diagram (d) for different light wavelengths $\lambda > \lambda_s$ and given ultrasound frequency f_s, distributions of light wavelength λ corresponding to exact phase matching (e) and spectral bandwidth $\Delta\lambda$ (FWHM) (f) across the circular FOV under the same conditions.

angular coordinates $(\delta\theta_{d1}, \delta\theta_{d2})$ and may be further transformed to pixel coordinates (u, v) in the image plane of a camera using the pinhole camera model.[29] The results of numerical modeling also showed that we can transform the distribution $f(\delta\theta_{i1}, \delta\theta_{i2})$ to $\lambda(\delta\theta_{i1}, \delta\theta_{i2})$ using the dependency $\lambda(f)$ for the axial ray without significant loss in accuracy.

In order to estimate the monochromatic field of view (FOV) or the spectral resolution, we should analyze the transmission function $T(\lambda, f, \delta\theta_{i1}, \delta\theta_{i2})$ of AOTF. The commonly used method introduces a wavevector mismatch $\mathbf{\Delta k}$ into the momentum conservation law: $\mathbf{k}_d = \mathbf{k}_i \pm \mathbf{q}_s + \mathbf{\Delta k}$. For given vectors $\mathbf{k}_i$ and $\mathbf{q}$, we can find the mismatch $|\mathbf{\Delta k}|$ as the distance from the end of the vector $(\mathbf{k}_i + \mathbf{q})$ to the nearest point on the wavevector surface for the ordinary wave and calculate the transmission function as follows:[27,30]

$$|\mathbf{\Delta k}(\lambda, f, \mathbf{e}_{ki}, \mathbf{e}_q)| = \min_{\mathbf{e}_{kd}} \left| [n_i(\lambda_{i0}, \mathbf{e}_{ki})/\lambda_{i0}]\,\mathbf{e}_{ki} + [f/V(\mathbf{e}_q)]\,\mathbf{e}_q - [n_d(\lambda_{d0}, \mathbf{e}_{kd})/\lambda_{d0}]\,\mathbf{e}_{kd} \right|, \tag{5}$$

$$T(\lambda, f, \mathbf{e}_{ki}, \mathbf{e}_q) = (\Gamma L_a)^2 \mathrm{sinc}^2\left(L_a \sqrt{\Gamma^2 + (|\mathbf{\Delta k}(\lambda, f, \mathbf{e}_{ki}, \mathbf{e}_q)|/2)^2} \right), \tag{6}$$

where $\mathrm{sinc}(x) \equiv (\sin x)/x$, Γ is a coupling coefficient proportional to the effective photoelastic constant and acoustic wave amplitude, L_a is a length of AO interaction. For (e→o) interaction, the equations for $|\mathbf{\Delta k}|$ may be derived analytically.[19,27] In our case, the direction of sound wavevector $\mathbf{e}_q$ is fixed according to the cut angle γ, so we can represent the transmission function from Eq. (6) in input angular coordinates $T(\lambda, f, \delta\theta_{i1}, \delta\theta_{i2})$. Afterwards, the frequency bandwidth Δf for each input direction $(\delta\theta_{i1}, \delta\theta_{i2})$ is defined as full width at half maximum (FWHM) and can be calculated from the condition $T(\lambda_s, f \pm \Delta f, \delta\theta_{i1}, \delta\theta_{i2}) = T(\lambda_s, f, \delta\theta_{i1}, \delta\theta_{i2})/2$,

where f corresponds to the exact syncronism for λ_s. The results of numerical modeling for paratellurite AO cell with the same parameters as before are shown in Fig. 2c. The actual length L_a of AO interaction was calculated using the length L of piezotransducer, the direction $\mathbf{s}_i$ and the angle ζ. The divergence of the acoustic beam was not considered. Similarly, the spectral bandwidth $\Delta\lambda\left(\delta\theta_{i1}, \delta\theta_{i2}\right)$ is estimated from $T\left(\lambda \pm \Delta\lambda, f_s, \delta\theta_{i1}, \delta\theta_{i2}\right) = T\left(\lambda, f_s, \delta\theta_{i1}, \delta\theta_{i2}\right)/2$, where λ corresponds to the exact phase matching for f_s, and presented in Fig. 2f. The calculated dependencies indicate that the values of Δf and $\Delta\lambda$ vary significantly with a change in $\delta\theta_{i2}$ and remain approximately constant with a change in $\delta\theta_{i1}$.

The results of numerical modeling reveal significant spatio-spectral inhomogeneity of the light beam filtered by AOTF. As can be seen in Fig. 2, the spectral bandwidths at the edges of circular FOV $\pm 5°$ differ about two times. The difference in central wavelengths of the spectral transmission window for the center and the edges of FOV reaches a value more than 3 times greater than the spectral bandwidth. Thus, using AOTF for spectral imaging applications do not provide a stack of truly monochromatic images $I\left(u, v, f\right)$, which should be taken into consideration at the earlier design stage as well as for the processing of the acquired spectral data.

3. EXPERIMENTAL STUDY OF AOTF-BASED SPECTRAL IMAGERS

3.1 Basic optical schemes of AOTF-based spectral imagers

There are two main types of optical schemes being used in AOTF-based imagers: collimating[23] (Fig. 3a) and confocal telecentric[31] (Fig. 3b). In the collimating scheme AOTF works with parallel bundles of rays, so the AO diffraction geometry is the same for all points across the entrance pupil of the optical system. The aperture stop of the input lens CL is projected onto the center of ultrasound beam inside the AO cell by the $4f$-system consisting of lenses L1 and L2. The stop S placed in the intermediate image plane may be used to control FOV. A pair of crossed polarizers P1 and P2 provide the desirable (e→o) interaction and may be absent if the FOV is small enough to avoid overlapping of diffracted and non-diffracted light beams. Since each parallel bundle of rays corresponds to a certain point of an object, each point of a resulting spectral image would have a different central wavelength of spectral transmission window, strictly repeating the spatio-spectral transmission function of AOTF.

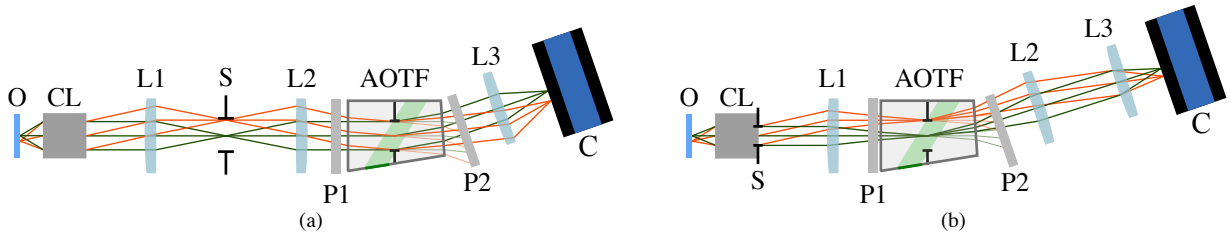

Figure 3. Collimating (a) and telecentric confocal (b) schemes of AOTF-based imagers. O, object; CL, collimating lens; S, stops; L1, L2, L3, lenses; P1, P2, polarizers; AOTF, acousto-optical tunable filter; C, camera.

For AOTF working in the confocal scheme, the center of ultrasound beam coincides with the intermediate image plane of the $4f$-system. Thus, the spectral selectivity for each image point is determined by the spatio-spectral transmission function averaged over all rays inside the angular aperture of the optical system. This allows to avoid significant variations of central wavelength over the FOV, but it also makes the structure of the acoustic field visible in the image as intensity perturbations. The aperture stop S allows to reduce the angular aperture and to avoid overlapping of diffracted and non-diffracted light beams similar to the collimating scheme.

3.2 Experimental setup

In order to demonstrate the appearance of the specific spatio-spectral structure of the light beam filtered by the AOTF on the images acquired by both collimating and confocal schemes, we have conducted a series of experiments using the wide-aperture AOTF based on TeO_2 crystal with the following parameters: cut angle

$\gamma = 7°$, back facet angle $\beta = 2.3°$, maximum linear aperture of 10 mm. It may be tuned to filter light wavelengths in 450...900 nm range using ultrasound frequencies from 130 to 65 MHz and average driving power about 1 W. Other elements of the experimental setup are listed as follows. The $4f$-system was composed of the custom achromatic doublets L1 ($f_1 = 18$ mm) and L2 ($f_2 = 30$ mm), P1 and P2 were film polarizers (XP42-200, Edmund Optics). Lens L3 (TBL 25, The Imaging Source) focused the diffracted beams onto the image sensor of monochrome camera C (DMK 37BUX178, The Imaging Source). First, we replaced object O and input lens CL by a monochromator (SF-46, LOMO) with a halogen light bulb and a diffusive plate to provide homogenous monochromatic light field suitable for transmission function measurements. Next, we put everything back in place and captured images of a color print illuminated by a fluorescent lamp with a line spetrum through CL (MD 135 mm f/2.8, Minolta) to provide an example of spatio-spectral image inhomogeneity.

3.3 Estimating the spatio-spectral inhomogeneity for collimating scheme

We acquired image stacks $I(u, v, f)$ of the homogeneous monochromatic light field tuning the acoustic frequency in the range from 60 to 115 MHz with 0.1 MHz step for several central wavelengths λ_{MC} of the monochromator ($\lambda_{\mathrm{MC}} = 525...700$ nm, 25 nm step) with slit width of 1 nm. The examples of captured images for $\lambda_{\mathrm{MC}} = 650$ nm are shown in Fig. 4a. Although the analyzed FOV is rather small ($\pm 2.4°$) as it is usually limited in AOTF-based spectral imagers, the inhomogeneity of image intensity is clearly visible as the bright circle at 78 MHz and the ring-like patterns at higher frequencies.

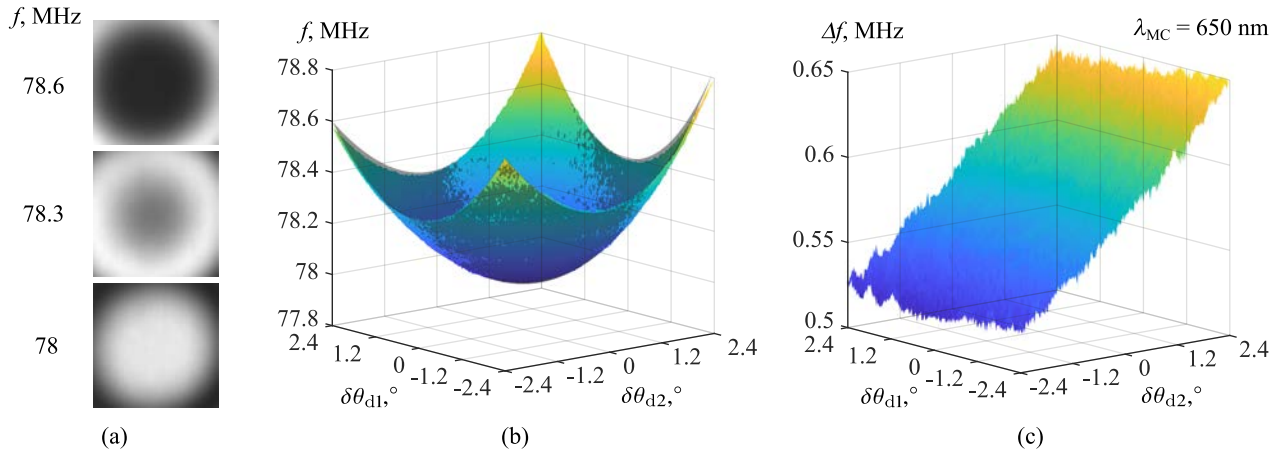

Figure 4. Spatio-spectral transmission of collimating AOTF-based imager. Examples of acquired images $I(u, v, f)$ (a). Experimental (color) and modeled (gray) dependencies of ultrasound frequency f with maximum transmission for $\lambda_{\mathrm{MC}} = 650$ nm on light angles after AOTF (b). Experimental distribution of frequency bandwidth Δf (FWHM) across FOV (c).

For each λ_{MC}, the set of images was processed to extract the dependency $f(u, v)$ corresponding to maximum values of $I(u, v, f)$ in each pixel. The experimentally obtained distribution was matched with the modeled one in the output angular coordinates $f(\delta\theta_{\mathrm{d1}}, \delta\theta_{\mathrm{d2}})$ using the least-squares fitting of the pinhole camera transformation $(u, v) \rightarrow (\delta\theta_{\mathrm{d1}}, \delta\theta_{\mathrm{d2}})$ and the minimum frequency f_{s} as additional free parameter. The result is shown in Fig. 4b: the experimental surface is filled with color, whereas the matched modeled surface is gray. The root-mean-square error (RMSE) for the whole FOV is about 0.01 MHz, so the experimental data matches the results of numerical modeling very well. The difference between the experimental and calculated values of minimum frequency f_{s} is about 1%, which may be caused by variations of refractive indices and sound phase velocities with temperature, uncertainty of cut angle and other parameters.

The image stacks $I(u, v, f)$ were also used to estimate the distribution of frequency bandwidth Δf (FWHM). The experimentally obtained surface demonstrated in Fig. 4c has the same shape as the calculated one (see Fig. 2c), but the absolute values of the experimental data are higher by about 10...15%. This may be explained by many factors, which were not considered for numerical modeling and lead to deviation of the transmission

function from approximation by sinc^2-function, such as spectral bandwidth of light from monochromator and acoustic beam divergence.

The experimentally obtained minimum frequency values f_s for each wavelength λ_MC were used to define the characteristic curve $\lambda(f)$ for the center of FOV (see Fig. 5a). Figure 5b demonstrates the experimental dependencies of frequency deviation range $(f\,(\mathrm{edge}) - f\,(\mathrm{center}))$ in two sections ($\delta\theta_{\mathrm{d}1} = 0$ and $\delta\theta_{\mathrm{d}2} = 0$) as well as the dependencies of frequency bandwidth Δf at the center and the edges of FOV on the light wavelength λ_MC. The characteristic curve $\lambda(f)$ was used to convert this values to the wavelength deviation ranges $(\lambda\,(\mathrm{edge}) - \lambda\,(\mathrm{center}))$ and spectral bandwidths $\Delta\lambda$ shown in Fig. 5c. Thus, the shift of the central wavelength of the spectral transmission window exceeds 3 nm at the edge of FOV in ($\delta\theta_{\mathrm{d}1} = 0$) section for $\lambda_\mathrm{MC} = 700$ nm and reaches even higher values in the corners of rectangular FOV. Although this spectral shift is about 1.5 times lower than the spectral bandwidth at the center of FOV, it may be significant for some applications. The wavelength deviation range grows more slowly than the spectral bandwidth with increasing wavelength because the frequency deviation range is smaller for longer wavelengths. The experimentally measured differences in spectral bandwidth across the FOV are ±10% of the FWHM value in the center of FOV.

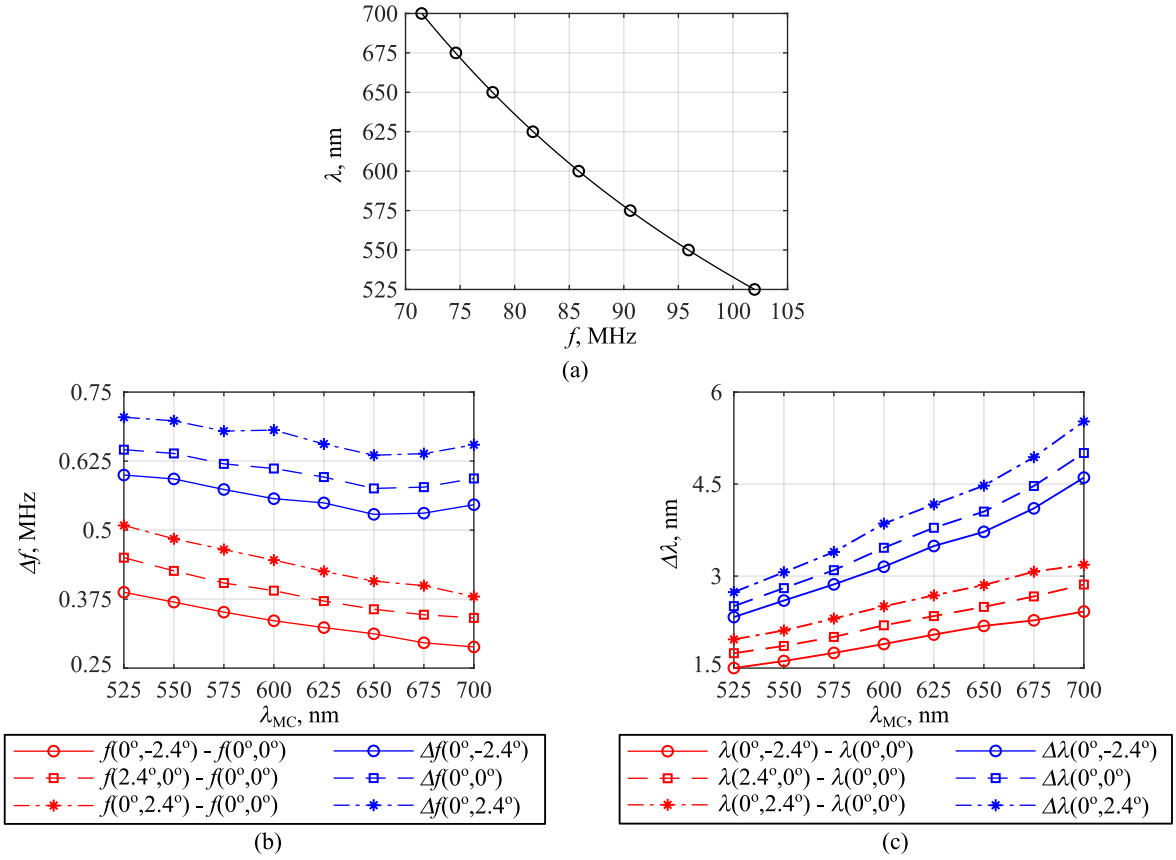

Figure 5. Estimation of spatio-spectral transmission inhomogeneity of collimating AOTF-based imager at different light wavelengths λ_MC. Experimentally obtained characteristic curve relating wavelength λ and frequency f with maximum transmission at the center of FOV (a). Experimental dependencies of frequency deviation $(f\,(\mathrm{edge}) - f\,(\mathrm{center}))$ at the edges of FOV (red) and frequency bandwidth Δf (FWHM, blue) at the center and the edges of FOV on light wavelengths λ_MC (b). Calculated dependencies of wavelength deviation $(\lambda\,(\mathrm{edge}) - \lambda\,(\mathrm{center}))$ (red) and spectral bandwidth $\Delta\lambda$ (FWHM, blue) on λ_MC (c).

3.4 Estimating the spatio-spectral inhomogeneity for confocal scheme

In the experiments with the confocal telecentric setup, the image stack $I(u, v, f)$ of the homogeneous monochromatic light field was captured at $\lambda_{\mathrm{MC}} = 650$ nm with the same slit width 1 nm and the same range of ultrasound frequencies. The examples of captured images shown in Fig. 6a reveal the wave-like pattern introduced by the imaged structure of the acoustic field. The experimentally measured distributions of ultrasound frequency $f(\delta\theta_{\mathrm{d1}}, \delta\theta_{\mathrm{d2}})$ corresponding to the maximum intensity value in each pixel and frequency bandwidth $\Delta f(\delta\theta_{\mathrm{d1}}, \delta\theta_{\mathrm{d2}})$ are presented in Figs. 6b and 6c. The results of the experiment indicate that both f and Δf remain approximately constant over the entire FOV, with standard deviations about 0.02 MHz and 0.01 MHz, respectively. The average spectral bandwidth $\Delta\lambda$ is 4.1 nm, which almost coincides with $\Delta\lambda$ for the collimating setup in the center of FOV.

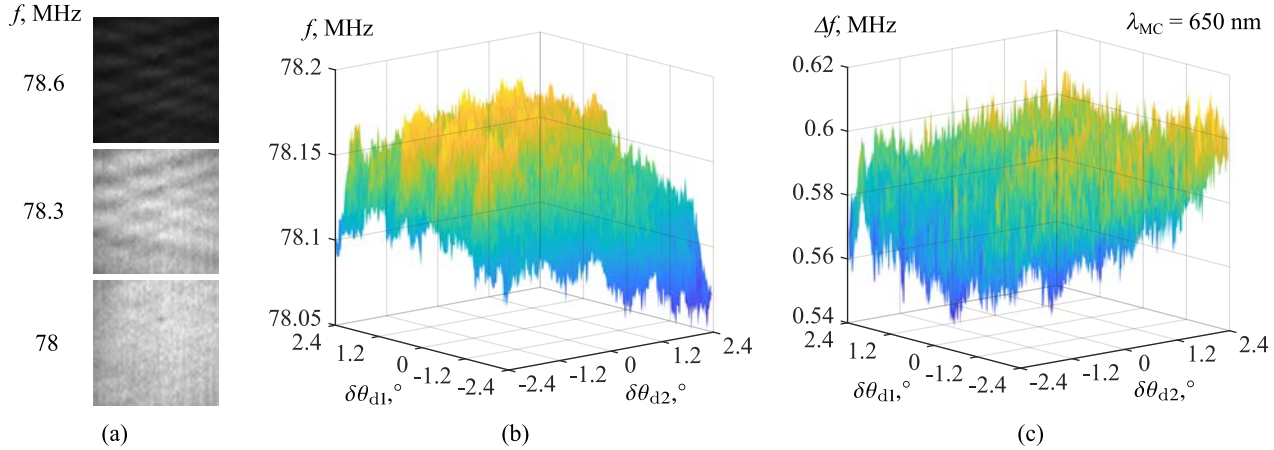

Figure 6. Spatio-spectral transmission of confocal AOTF-based imager. Examples of acquired images $I(u, v, f)$ (a). Experimentally measured dependencies of ultrasound frequency f with maximum transmission for $\lambda_{\mathrm{MC}} = 650$ nm (b) and frequency bandwidth Δf (FWHM) (c) on light angles after AOTF.

3.5 Imaging performance

To demonstrate the appearance of the AOTF transmission function inhomogeneity on the images, we captured image stack $I(u, v, f)$ of the color print illuminated by a fluorescent lamp with a line spectrum (see Figs. 7a and 7b) using both schemes. Figures 7c–e show the examples of images acquired with collimating setup at the sound frequencies corresponding to the wavelengths around clearly distinguishable line at 611.5 nm. We used the experimentally measured dependency $f(u, v)$ for $\lambda_{\mathrm{MC}} = 611.5$ nm to process the acquired image stack $I(u, v, f)$ and extract monochromatic image $I_{\mathrm{m}}(u, v)$. The corrected image (Fig. 7f) has no traces of circular or ring-like patterns visible in raw images and is not inferior in quality to the raw image captured by the confocal setup (Fig. 7g).

4. CONCLUSION

We have experimentally estimated the spatio-spectral inhomogeneity of the AOTF transmission and showed that the variations of central wavelength and spectral bandwidth are noticeable for collimating scheme of AOTF-based imager even in the commonly used small FOV. These variations arise from the phase matching condition and may be predicted in advance if the AO diffraction geometry and the parameters of crystal (such as refractive indices and sound velocities) are known. The stack of images captured by collimating AOTF-based imager can be processed to correct variations of central wavelength and extract monochromatic images, which are not worse than images captured by confocal setup. The findings of the work are applicable not only to paratellurite, but also to other uniaxial birefringent crystals. The obtained results may be useful for the design of AOTF-based hyperspectral imaging devices as well as for the development of spectral image processing techniques.

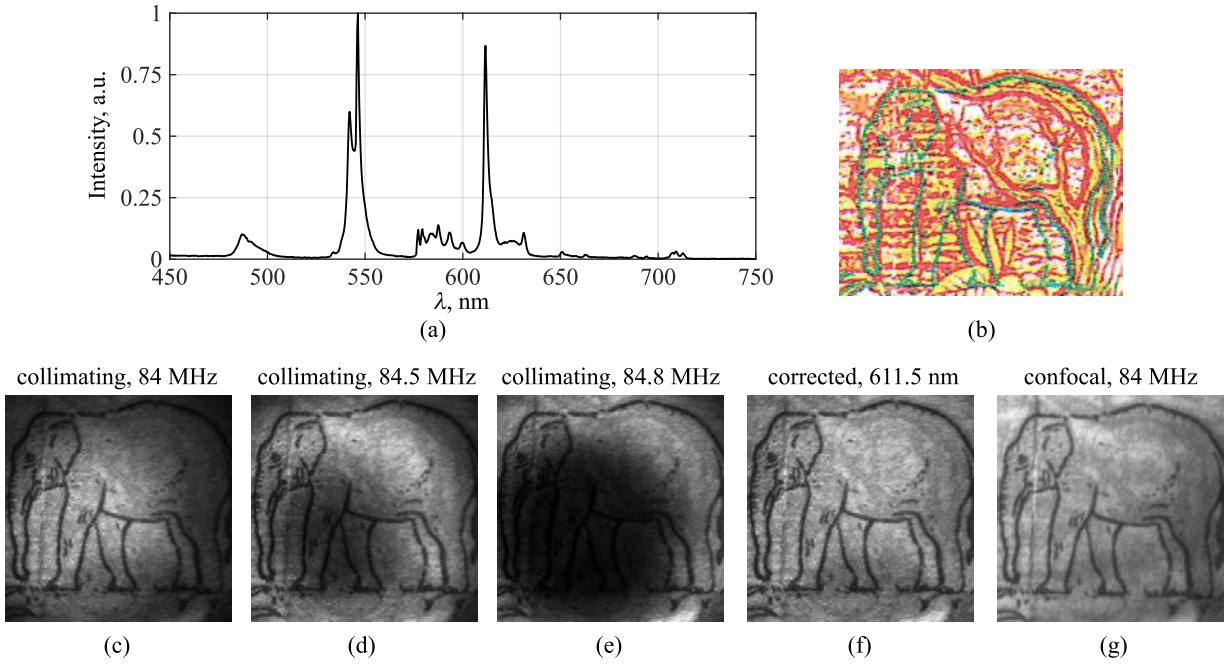

Figure 7. Spectral images of a color print lit by a fluorescent lightbulb with a line spectrum. Fluorescent lamp spectrum used to lit the test object (a). Scanned image of color print (b). Raw images captured by collimating AOTF-based imager tuned to 84 MHz (c), 84.5 MHz (d) and 84.8 MHz (e). Monochromatic image at $\lambda = 611.5$ nm obtained by post-processing a stack of images acquired by collimating imager (f). Image captured by confocal imager tuned to 84 MHz (g).

ACKNOWLEDGMENTS

The work has been supported by the Russian Science Foundation (project 19-19-00606).

REFERENCES

[1] Chang, I., "Acousto-optic devices and applications," *Handbook of optics* **2**, 12–1 (1976).

[2] Treado, P. J., Levin, I. W., and Lewis, E. N., "High-Fidelity Raman Imaging Spectrometry: A Rapid Method Using an Acousto-Optic Tunable Filter," *Appl Spectrosc* **46**, 1211–1216 (1992).

[3] Wachman, E. S., Niu, W.-h., and Farkas, D. L., "Imaging acousto-optic tunable filter with 0.35-micrometer spatial resolution," *Appl. Opt.* **35**, 5220 (1996).

[4] Inoue, Y. and Peñuelas, J., "An AOTF-based hyperspectral imaging system for field use in ecophysiological and agricultural applications," *International Journal of Remote Sensing* **22**, 3883–3888 (2001).

[5] Voloshinov, V. B., Yushkov, K. B., and Linde, B. B. J., "Improvement in performance of a TeO2 acousto-optic imaging spectrometer," *J. Opt. A: Pure Appl. Opt.* **9**, 341–347 (2007).

[6] Wachman, E. S., Geyer, S. J., Recht, J. M., Ward, J., Zhang, B., Reed, M., and Pannell, C., "Simultaneous imaging of cellular morphology and multiple biomarkers using an acousto-optic tunable filter–based bright field microscope," *J. Biomed. Opt* **19**, 056006 (2014).

[7] Pannell, C. N., Ward, J. D., Wachman, E. S., Zhang, B. G., and Reed, M. K., "A high-performance passband-agile hyperspectral imager using a large aperture acousto-optic tuneable filter," in [*Photonic Instrumentation Engineering II*], Soskind, Y. G. and Olson, C., eds., **9369**, 21 – 34, International Society for Optics and Photonics, SPIE (2015).

[8] Gao, Y., Zhou, M., Li, Q., Liu, H., and Zhang, Y., "AOTF based molecular hyperspectral imaging system and its image pre-processing method," in [*2015 8th International Conference on Biomedical Engineering and Informatics (BMEI)*], 14–18, IEEE, Shenyang, China (2015).

[9] Yushkov, K. B. and Molchanov, V. Y., "Hyperspectral imaging acousto-optic system with spatial filtering for optical phase visualization," *J. Biomed. Opt* **22**, 066017 (2017).

[10] Belyaev, D. A., Yushkov, K. B., Anikin, S. P., Dobrolenskiy, Y. S., Laskin, A., Mantsevich, S. N., Molchanov, V. Y., Potanin, S. A., and Korablev, O. I., "Compact acousto-optic imaging spectro-polarimeter for mineralogical investigations in the near infrared," *Optics Express* **25**, 25980 (2017).

[11] Korablev, O. I., Belyaev, D. A., Dobrolenskiy, Y. S., Trokhimovskiy, A. Y., and Kalinnikov, Y. K., "Acousto-optic tunable filter spectrometers in space missions [Invited]," *Appl. Opt.* **57**, C103 (2018).

[12] Kozun, M. N., Bourassa, A. E., Degenstein, D. A., and Loewen, P. R., "A multi-spectral polarimetric imager for atmospheric profiling of aerosol and thin cloud: Prototype design and sub-orbital performance," *Rev. Sci. Instrum.* **91**, 103106 (2020).

[13] Batshev, V., Machikhin, A., Martynov, G., Pozhar, V., Boritko, S., Sharikova, M., Lomonov, V., and Vinogradov, A., "Polarizer-Free AOTF-Based SWIR Hyperspectral Imaging for Biomedical Applications," *Sensors* , 10 (2020).

[14] Balakshy, V. I., Parygin, V. N., and Chirkov, L. E., [*Physical principles of acousto-optics*], Radio i Svyaz, Moscow (1985).

[15] Balakshy, V. I. and Kostyuk, D. E., "Acousto-optic image processing," *Appl. Opt.* **48**(7), C24–C32 (2009).

[16] Kotov, V. M., "Processing of 2D Images Using the Bragg Diffraction," *J. Commun. Technol. Electron.* **65**, 1331–1335 (2020).

[17] Yushkov, K. B., Chizhikov, A. I., Makarov, O. Y., and Molchanov, V. Y., "Optimization of noncollinear AOTF design for laser beam shaping," *Appl. Opt.* **59**, 8575 (2020).

[18] Goutzoulis, A. P. and Pape, D. R., eds., [*Design and fabrication of acousto-optic devices*], Marcel Dekker, N.Y. (1994).

[19] Gorevoy, A. V., Machikhin, A. S., Martynov, G. N., and Pozhar, V. E., "Spatiospectral transformation of noncollimated light beams diffracted by ultrasound in birefringent crystals," *Photon. Res.* **9**, 687–693 (2021).

[20] Krauz, L., Páta, P., Bednář, J., and Klíma, M., "Quasi-collinear IR AOTF based on mercurous halide single crystals for spatio-spectral hyperspectral imaging," *Opt. Express* **29**, 12813–12832 (2021).

[21] Epikhin, V. M., Vizen, F. L., and Pal'tsev, L. L., "Acoustooptic filtering of radiation with arbitrary polarization," *Zhurnal Tekhnicheskoi Fiziki* **57**, 1910–1917 (1987).

[22] Machikhin, A., Batshev, V., Pozhar, V., Naumov, A., and Gorevoy, A., "Acousto-optic tunable spectral filtration of stereoscopic images," *Opt. Lett.* **43**, 1087–1090 (2018).

[23] Machikhin, A., Batshev, V., and Pozhar, V., "Aberration analysis of AOTF-based spectral imaging systems," *J. Opt. Soc. Am. A* **34**(7), 1109–1113 (2017).

[24] Zhao, H., Li, C., and Zhang, Y., "Three-surface model for the ray tracing of an imaging acousto-optic tunable filter," *Appl. Opt.* **53**, 7684 (2014).

[25] Cojocaru, E., "Direction cosines and vectorial relations for extraordinary-wave propagation in uniaxial media," *Appl. Opt.* **36**, 302–306 (1997).

[26] Voloshinov, V. B., "Anisotropic light diffraction on ultrasound in a tellurium dioxide single crystal," *Ultrasonics* **31**(5), 333–338 (1993).

[27] Pozhar, V. and Machihin, A., "Image aberrations caused by light diffraction via ultrasonic waves in uniaxial crystals," *Appl. Opt.* **51**, 4513 (2012).

[28] McNeill, M. D. and Poon, T.-C., "Gaussian-beam profile shaping by acousto-optic Bragg diffraction," *Appl. Opt.* **33**(20), 4508–4515 (1994).

[29] Hartley, R. I. and Zisserman, A., [*Multiple view geometry in computer vision*], Cambridge University Press, Cambridge, 2nd ed. (2004).

[30] Yariv, A. and Yeh, P., [*Optical waves in crystals*], vol. 5, Wiley New York (1984).

[31] Suhre, D. R., Denes, L. J., and Gupta, N., "Telecentric confocal optics for aberration correction of acousto-optic tunable filters," *Appl. Opt.* **43**(6), 1255–1260 (2004).